Journal of Applied Fluid Mechanics, Vol. 18, No. 4, pp. 947-959, 2025.
Available online at www.jafmonline.net, ISSN 1735-3572, EISSN 1735-3645.
https://doi.org/10.47176/jafm.18.4.3052

Numerical Simulations of the Effect on Aerodynamic Performances of the Inter-propeller Distance in a Contra-rotating Propeller

H. Bentrad[1†], H. Moulai[1], A. Bekhti[2] and S. Laâzab[1]

[1] *University of Saâd Dahleb Blida 1, Ouled Yaïch, Blida, 09100, Algeria*
[2] *Renewable Energies Development Centre, Bouzareah, Algiers, 16340, Algeria*

†Corresponding Authors Emails: bentrad_hocine@univ-blida.dz

ABSTRACT

We investigate the aerodynamics of low-Reynolds-number contrarotating propellers (CRPs) through numerical simulations. This field has gained increasing relevance owing to advancements in unmanned aerial vehicle technologies. The primary objective of this study was to evaluate the effect of interpropeller distance on the aerodynamic performance of CRPs, measured using the thrust coefficient (C_T), power coefficient (C_P), and efficiency (η). Transient three-dimensional computational fluid dynamics simulations employing the unsteady Reynolds-averaged Navier–Stokes equations coupled with the k–ε turbulence model were conducted on an isolated propeller at various advance ratios. The results were then compared with the experimental data from a similarly shaped propeller. Simulations of different CRP interpropeller distances were performed with OpenFOAM software. The results indicated that increasing the interpropeller distance significantly enhances thrust, with a corresponding slight increase in efficiency.

Article History

Received August 17, 2024
Revised November 27, 2024
Accepted December 13, 2024
Available online February 4, 2025

Keywords:

UAV
OpenFOAM
CFD
Propeller spacing
Propeller aerodynamics

1. INTRODUCTION

The quest for efficient and reliable propulsion systems is crucial for both economic and environmental sustainability, and has attracted the attention of industries and researchers. As aircraft design evolves to meet the increasing demand for efficiency and reduced emissions, several plane designs that integrate driven propeller engines, particularly contrarotating propellers (CRPs), are gaining prominence. CRPs consist of two coaxially aligned propellers rotating in opposite directions, and the prescribed configuration provides the benefit of thrust augmentation and negates the reaction torque. These advantages are particularly interesting for unmanned aerial vehicle (UAV) applications and offer an appealing alternative.

Propellers have been extensively studied since the beginning of aeronautics; however, studies on propellers in general, and CRPs in particular, are still being conducted and can be divided into three areas:

I) Non-computational fluid dynamics (non-CFD) numerical methods, such as in the work of Grassi et al. (2010), where the authors compared the latest numerical methods at the time, one using the lifting line theory for the design and another using the lifting surface theory for the performance, in the case of a CRP setup with experimental results from cavitation tunnel tests. They obtained a satisfactory agreement between the numerical and experimental results. Thiele et al. (2019) proposed a blade element momentum theory method to evaluate the performance of single- and counter-rotating UAV propellers. The model showed promising results in various flow configurations; however, it is still limited because it does not compute the trailing vortices and wake effects.

II) Experimental measurements, such as those of Brandt and Selig (2011), who conducted an experimental study on 79 low-Reynolds-number propellers for UAVs. They observed that the effect of low-Reynolds-number conditions is significant and degrades propeller performance. They reported efficiencies ranging from 0.28 (for a poor propeller) to a peak near 0.65. Silvestre et al. (2015) also conducted experimental tests on low-Reynolds-number propellers and reached the same conclusion concerning the decrease in performance with a decrease in the rotational speed. Russo et al. (2023) performed an experimental investigation on the CRP for UAV applications. Their experimental setup did not allow for a study considering various advance coefficients; therefore, the rotational velocity was considered instead to

NOMENCLATURE

Latin Alphabet

C_P	power coefficient
C_Q	torque coefficient
c_{ref}	chord of reference
C_T	thrust coefficient
d	inter-propeller distance
D	diameter
J	advance ratio
k	turbulent kinetic energy
N	rotational speed (in revolutions per second)
p	pressure
P	power
Q	torque
R_{ij}	Reynolds Stress Tensor
t	time variable
T	thrust
St	Strouhal number
u	velocity
V	free stream or cruising velocity
x	spatial variable

Greek Alphabet

ε	turbulent dissipation energy
μ	dynamic viscosity
μ_t	turbulent (eddy) dynamic viscosity
η	efficiency
κ	Von Karman constant
ρ	density
τ	shear stress
φ	frequency
ω	vorticity

Subscripts

aft	afterward
fwd	forward
i	spatial index
j	spatial index
k	spatial index

Abbreviations

aft	Afterward
AMI	Arbitrary Mesh Interface
CFD	Computational Fluid Dynamics
CRP	Contra-rotating Propeller
Fwd	Forward
MRF	Multiple Reference Frame
RANS	Reynolds Averaged Navier-Stokes
rpm	Revolutions Per Minute
UAV	Unmanned Aerial Vehicles

differentiate between cases (equivalent to hover). They observed that the overall thrust did not vary significantly with the spacing between propellers; however, the thrust of individual propellers was significantly affected with a single propeller, outperforming the individual propellers in the CRP configurations.

III) The CFD, which is the focus of the present study.

The CFD investigations of single propellers have been extensively conducted, and some published studies are presented as follows:

Stajuda et al. (2016) performed a CFD investigation using the multiple reference frame (MRF) approach for a dual-bladed propeller, and the results were compared with those of experiments. They used the Reynolds-averaged Navier–Stokes (RANS) shear stress transport (SST) k–ω model to compute their results. The main advantage of this approach is its ability to conduct steady flow simulations. However, the authors showed that the results were very sensitive to the rotating domain thickness when using the MRF technique.

Triet et al. (2018) used the k–ε turbulence model and the MRF approach with the OpenFOAM software to analyze a three-bladed marine single propeller. The results showed good agreement with experiments for low advance ratios (less than 0.7).

Stokkermans et al. (2018) examined the capabilities of different modeling methods in a RANS solver for isolated and wing-mounted propellers. The use of actuator-disk and actuator-line models to reduce the computational cost was also investigated by applying blade-loading results extracted from simulations in which the blades were fully resolved. The simulations were compared with experiments. It was concluded that the Spalart–Allmaras equation is sufficient to predict the behavior of the propeller provided a sufficiently refined grid (the numerical errors can also be reduced via local refinements), whereas the other methods also provide good results with a reduction in the computational time. However, although these methods provide good predictions of propeller performance, they do not allow obtaining the entire field data, which is essential for understanding the flow mechanisms involved.

CRP configurations have also been considered, and several studies have been conducted within the framework of this concept.

Feng et al. (2017) used the SST k–ω turbulence model to evaluate the hydrodynamic performance of a four-bladed marine CRP with the Star-CCM+ software; they used the MRF approach and a fully structured grid. They compared numerical results with experiments, and the results showed a fair agreement.

Su et al. (2019) investigated the single, tandem, and CRP configurations for marine applications. They used the standard k–ε, k–ε renormalization group, SST k–ω, and Reynolds stress modeling (RSM) turbulence models to assess the performance. A comparison with experiments showed that the RSM model is the most accurate, whereas the error of the standard k–ε model is the largest. Among the three configurations, the CRP configuration showed the highest efficiency.

Wenhui and Kun (2023) investigated the effects of axial spacing in a six-bladed aircraft CRP using the unsteady RANS SST k–ω turbulence model and sliding mesh technique at an advance ratio of J=2.5. This study highlighted the importance of spacing in CRP design. The authors observed that, from four study cases, the one with a spacing of 0.25D yielded a higher overall efficiency.

Lopez and Juando (2023) performed simulations using OpenFOAM on various CRP configurations (for applications in hydrofoil vessels) by varying the number of blades and propeller diameters. Blade imbalance was observed to be helpful, as it minimized the likelihood of resonance, and a smaller diameter for the aft propeller was also recommended to exploit the induced velocity effect while avoiding trailing tip vortices. The authors also suggested minimizing the spacing between propellers.

Xu et al. (2024) used the SST k–ω model with the MRF technique to investigate the flow around a CRP for an electric vertical takeoff and landing (eVTOL) human transport application. The primary objective was to assess the lift losses of the aft propeller owing to the downwash effect of the forward propeller at hover for multiple rotational speeds. Their findings indicated that the lift loss of the CRP system ranged from 35.28% to 38.85%. Therefore, this effect must be considered in the design phase.

Regarding multirotor configurations, Pérez et al. (2019) aimed to predict the performance of a quadrotor configuration. The authors used both the unsteady vortex lattice method and the SST k–ω model with the MRF technique, and compared both approaches with experimental data (for a single rotor). The unsteady vortex lattice method overestimated the figure of merit (or static efficiency), whereas the CFD results were similar to the experimental data.

Azizan & Sapit (2022) also performed a CFD study with quadrotor applications. They investigated the influence of the blade twisting angle on the performance using the realizable k–ε model. If the propellers have a fixed pitch, the authors recommend the use of moderate twisting angles, because they are suitable for the high rotational speeds required for hovering in the case of quadrotors.

The aforementioned publications highlight that CRP aerodynamics is a very active research field, where it is difficult to reach broad conclusions owing to the variety and intricacy of potential cases. The performance is very sensitive to changes in conditions, making further research worthwhile.

This study aimed to develop a more sustainable and economical propulsion technology (with a specific application in UAVs) through a comprehensive study of CRPs using CFD. The main aim of this study was to assess the influence of the axial spacing between the two propellers on the efficiency of the system.

2. MATHEMATICAL FORMULATION

Transient three-dimensional numerical simulations were performed. The air flow was assumed to be incompressible and was modeled using the unsteady RANS (URANS) equations coupled with the $k-\varepsilon$ turbulence model (Launder & Spalding, 1974). Using Cartesian coordinates, the index notation, and Einstein's sum convention, the governing equations are as follows:

- The continuity equation:

$$\frac{\partial \overline{u_\iota}}{\partial x_i} = 0 \tag{1}$$

- The momentum equation:

$$\rho\left(\frac{\partial \overline{u_\iota}}{\partial t} + \overline{u_k}\frac{\partial \overline{u_\iota}}{\partial x_k}\right) = -\frac{\partial \bar{p}}{\partial x_i} + \frac{\partial}{\partial x_j}\left(\mu\frac{\partial \overline{u_\iota}}{\partial x_j}\right) + \frac{\partial}{\partial x_j}R_{ij} \tag{2}$$

Here, ρ is the fluid density, u_i is the velocity across the x_i direction, p is the pressure, and R_{ij} represents the Reynolds stress tensor.

$$R_{ij} = -\rho\overline{u_i'u_j'} \tag{3}$$

The bars above a variable denote that it is averaged (such as $\overline{u_\iota}$), whereas values with prime symbols (such as u_i') represent fluctuations. To close the system, the two-equation $k-\varepsilon$ model (Launder & Spalding, 1974) was used. It consists of the transport equations of the turbulent kinetic energy k and dissipation rate ε.

$$\frac{D\varepsilon}{Dt} = \frac{1}{\rho}\frac{\partial}{\partial x_k}\left[\frac{\mu_t}{\sigma_1}\frac{\partial \varepsilon}{\partial x_k}\right] + \frac{C_1\mu_t}{\rho}\frac{\varepsilon}{k}\left(\frac{\partial u_i}{\partial x_k} + \frac{\partial u_k}{\partial x_i}\right)\frac{\partial u_i}{\partial x_k} - C_2\frac{\varepsilon^2}{k} \tag{4}$$

$$\frac{Dk}{Dt} = \frac{1}{\rho}\frac{\partial}{\partial x_k}\left[\frac{\mu_t}{\sigma_2}\frac{\partial k}{\partial x_k}\right] + \frac{\mu_t}{\rho}\left(\frac{\partial u_i}{\partial x_k} + \frac{\partial u_k}{\partial x_i}\right)\frac{\partial u_i}{\partial x_k} - \varepsilon \tag{5}$$

The turbulent viscosity μ_t was computed using the following relation:

$$\mu_t = \rho C_\mu \frac{\bar{k}^2}{\bar{\varepsilon}} \tag{6}$$

and the Boussinesq eddy viscosity assumption was used to compute the Reynolds stress tensor:

$$R_{ij} = -\rho\overline{u_i'u_j'} = \mu_t\left(\frac{\partial \overline{u_\iota}}{\partial x_j} + \frac{\partial \overline{u_j}}{\partial x_i}\right) - \frac{2}{3}\mu_t\frac{\partial \overline{u_k}}{\partial x_k}\delta_{ij} - \frac{2}{3}\rho k\delta_{ij} \tag{7}$$

The values of the empirical constants C_μ, C_1, C_2, σ_k, and σ_ε of the model are presented in Table 1.

The described model presents a fully turbulent case, and standard wall functions were used to consider the wall adhesion effect.

To evaluate the aerodynamic performance of the tested configurations, the following dimensionless coefficients, which originate from the dimensional analysis, were introduced for a single propeller:

- The advance ratio J:

$$J = \frac{V}{ND} \tag{8}$$

Table 1 Turbulence model constants

C_μ	C_1	C_2	σ_1	σ_2
0.09	1.44	1.92	1.0	1.2

- The thrust coefficient C_T:

$$C_T = \frac{T}{\rho N^2 D^4} \tag{9}$$

- The torque coefficient C_Q:

$$C_Q = \frac{Q}{\rho N^2 D^5} \tag{10}$$

- The power coefficient C_P:

$$C_P = \frac{P}{\rho N^3 D^5} = 2\pi C_Q \tag{11}$$

Furthermore, for CRPs, the coefficients can be written as follows:

$$C_T = \frac{T_{fwd} + T_{aft}}{\rho 0.25\left(N_{fwd}^2 + N_{aft}^2\right)\left(D_{fwd}^4 + D_{aft}^4\right)} \tag{12}$$

$$C_Q = \frac{Q_{fwd} + Q_{aft}}{\rho 0.25\left(N_{fwd}^2 + N_{aft}^2\right)\left(D_{fwd}^5 + D_{aft}^5\right)} \tag{13}$$

$$C_P = \frac{P_{fwd} + P_{aft}}{\rho 0.25\left(N_{fwd}^3 + N_{aft}^3\right)\left(D_{fwd}^5 + D_{aft}^5\right)} \tag{14}$$

The propulsive efficiency η of a nonstatic propeller is defined as the ratio between the useful power (which is the thrust T multiplied by the cruising or free stream velocity V) and the power given to the propeller by the shaft (which is the torque Q multiplied by the rotational speed $2\pi N$). The propulsive efficiency η is defined as follows:

$$\eta = \frac{TV}{P} = \frac{C_T J}{C_P} \tag{15}$$

3. NUMERICAL METHODOLOGY

Simulations for the grid sensitivity analysis were performed using ANSYS Fluent on a Xeon E5-1650 v2 with 128 GB of RAM. The MRF technique was used, and a steady regime was assumed to reduce the computational time. For the simulations of the studied transient test cases, the sliding mesh technique was used with OpenFOAM on an i7 10700H processor with 32 GB of RAM. The same boundary conditions and settings were used for both the machines.

The PIMPLE solver, which is a coupled SIMPLE–PISO incompressible solver, is used in OpenFOAM. Simulations were performed with second-order discretization schemes (Gaussian linear upwind for divergence and least squares for gradient) for the spatial terms, and the implicit Euler formulation was used for time discretization. Residuals were maintained under 10^{-5} for pressure and 10^{-6} for the other variables, and the adaptive time-step concept was utilized according to a maximum Courant number of 25. This is justifiable because the zone where the Courant number exceeds unity is very small compared with the propeller. The application of an adaptive time-stepping strategy avoids the occurrence of instability, which yields time steps on the order of 10^{-5} corresponding to less than 0.035° of rotation,

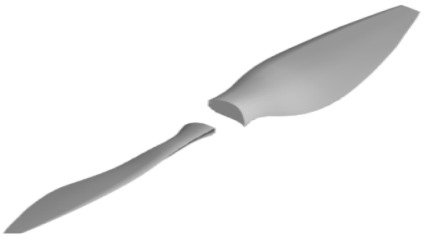

Fig. 1 Propeller geometry

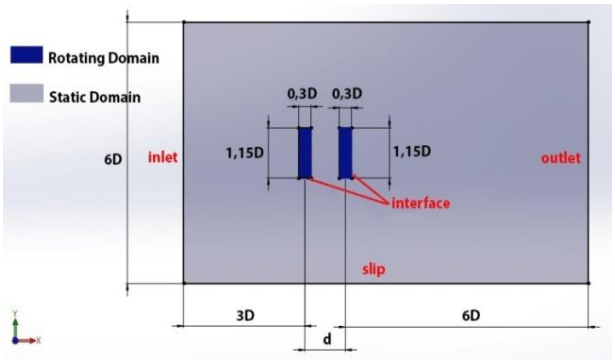

Fig. 2 Sketch of the computational domain

which is in accordance with the time-step size recommended by Satrio et al. (2018).

3.1. Geometry and Computational Domain

The computational domain was generated using Gambit v 2.4.6, which is a software under the ANSYS umbrella that allows the creation of geometries and computational grids.

The propeller has a diameter D=0.34 m, a reference setting angle of 20°, and a reference chord (located at three quarters of the radius starting from the hub) of 2.84 cm. The geometry is available at https://grabcad.com/library/low-reynolds-propeller-for-ultra-light-aircrafts-1 and is shown in Fig. 1.

The hub of the propeller was neglected to obtain a higher mesh quality and facilitate convergence; hence, only the blade effects were considered.

The computational domain consisted of a cylinder split into two subdomains for the isolated propeller case (an outer static domain and an inner rotating domain) and into three subdomains for the CRP configuration cases.

The sketch illustrated in Fig. 2 is a dimensionless representation of a slice of the computational domain in the (x, y) plane, where the forward (fwd) propeller is placed at the origin with the relevant boundary conditions, and the aft propeller is placed at a distance d from the fwd propeller, where d varies from 0.3D to 1D. The same computational domain was used for a single propeller.

For the boundary conditions, a constant-velocity inlet, constant-pressure outlet, and slip wall were used at the outer bounds of the computational domain (Fig. 2), and an arbitrary mesh interface was used between the rotating and static domains. The blades of the propeller were considered as no-slip walls, and the rotating domain

Table 2 Computational grids total number of cells

	Number of cells		
	Rotating domain	Static domain	Whole domain
Grid 1	427,859	711,880	1,139,739
Grid 2	471,859	1,105,850	1,577,630
Grid 3	631,735	1,602,250	2,233,985
Grid 4	754,747	1,787,250	2,541,997

Table 3 Total number of cells for the different simulated configurations

Isolated Propeller	CRP with d=0.3	CRP with d=0.5	CRP with d=1.0
1,577,630	2,149,410	2,266,730	2,374,592

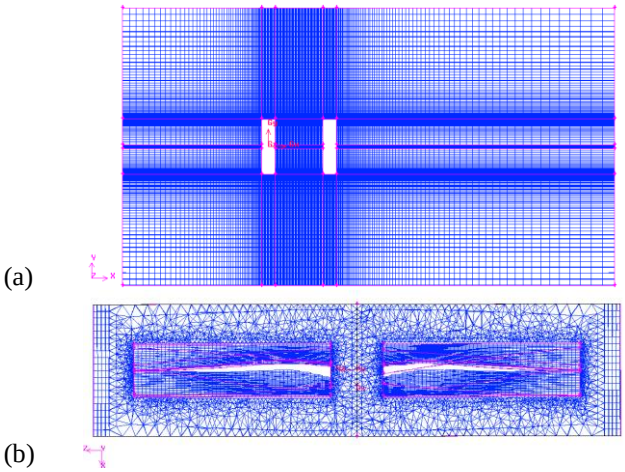

Fig. 3 Slice of the computational grid of (a) the static domain for the CRP cases and (b) the rotating domain for all cases

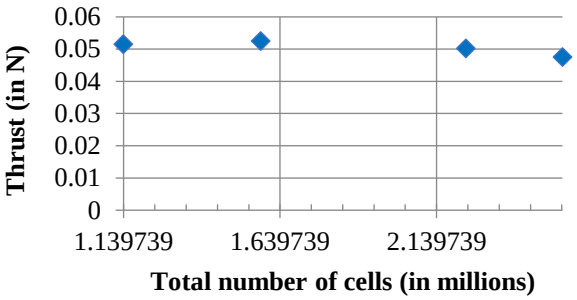

Fig. 4 Variation of thrust with respect to the total number of cells

(where the blades are enclosed) rotated at the propeller rpm, which ranged from 191 to 573 rpm. The highest simulated rotational speed yielded a tip velocity of 10.2 m/s, which is in accordance with the incompressible fluid assumption.

The initial fields were assumed to be uniform and had zero values for all the parameters.

3.2. Computational Grid

The computational grid was generated using Gambit v. 2.4.6. A fully structured hexahedral grid was used in the static domain. The grid was refined at the proximity of the rotating domain, with emphasis placed on the radial interface between them. Fig. 3 (a) shows a slice of the cylindrical static domain at plane z=0 for the CRP case.

The grid was particularly refined in the interpropeller region to capture any interaction that influences the performance. The same meshing approach was adopted for the isolated propeller.

However, in the rotating domain (common to the isolated propeller and CRP cases), a hybrid approach was adopted. Near the blades and radial interface, a fully structured hexahedral grid was used with the value of y+ maintained between 30 and 160 for all the cases, considering that a standard wall function is used for near-wall treatment (Greenshields, 2015, Liu et al., 2017). Tetrahedral cells were adopted for the remainder of the domain, as shown in Fig. 3 (b).

3.3. Grid Sensitivity analysis

To assess the grid sensitivity, four different grids were tested, ranging from a coarse grid (≈1.1 million cells) to a fine grid (≈2.5 million cells), as shown in Error! Not a valid bookmark self-reference.. A grid sensitivity analysis was performed only for the isolated propeller case (to shorten the computational time), with the chosen grid being transposed to the CRP cases. For each grid, refinements were made in the rotating domain and the wake zone downstream of the propeller in the static domain.

The value of thrust was used for the grid sensitivity assessment at an advance ratio of J=0.462 and an inlet velocity of 1 m/s. Fig. 4 shows the value of thrust (in N) as a function of the total number of elements.

As the tested grids yielded similar results, a grid containing 1.578 million elements was chosen for all the simulations. This number increased with the CRP configuration, as indicated in Table 3.

4. RESULTS

4.1. Isolated Propeller

CFD simulations were performed for six advance ratios (J=0.308, J=0.462, J=0.616, J=0.738, J=0.84, and J=0.94) with an imposed free-stream velocity of 1 m/s for the isolated propeller. The results were compared with the

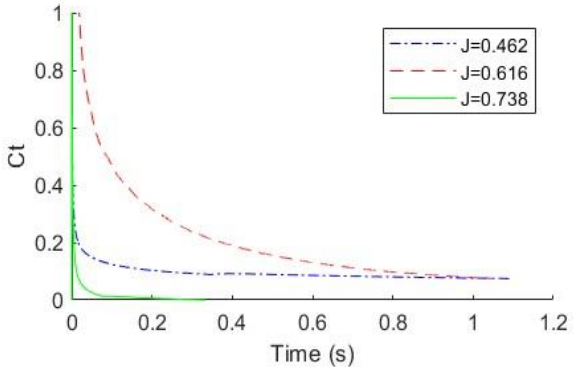

Fig. 5 Variation of the thrust coefficient with time for an isolated propeller at multiple advance ratios

experimental data (Brandt & Selig, 2011) of the closest commercial propeller in terms of geometry (Graupner CAM Slim 10x8) at 3,000 rpm. However, as the results were taken in a dimensionless form, they were assumed to be equivalent because the change in the Reynolds number was sufficiently small for dynamic similarity.

All the parameters tended to converge toward a stable sustained state, although for the advance ratio of J=0.616, a sustained regime was not attained until the fifth revolution. The convergence rate is illustrated in Fig. 5, where the thrust coefficient is represented as a function of time for different advance ratios. Similar variations were observed in the power coefficient and efficiency.

To study the performance, the average values of the characteristic coefficients over the last revolution of the propeller were considered, and tendency curves were used to perform the analysis.

Figure 6 (a) shows the variation in the thrust coefficient with respect to the advance ratio. The results from the CFD simulations and the experimental data (Brandt & Selig, 2011) are also shown. All the presented data exhibited the same behavior: the thrust coefficient decreased with an increase in the advance ratio in a quasilinear manner. However, the CFD results differed in that the slope of the thrust coefficient was more pronounced; indeed, the values were overestimated for low advance ratios, which is consistent with previous studies (Rhee & Joshi, 2005; Su et al., 2019), and underestimated for high advance ratios.

Concerning the power coefficient, a similar general behavior can be observed in Fig. 6 (b). However, for the same advance ratio, the C_P was overestimated (approximately double). The overprediction of C_P is a known consequence of using the k–ε model (Rhee & Joshi, 2005; Colley & Gourlay, 2012; Su et al., 2019)

The difference between the CFD simulations and the experimental data was most evident in the efficiency obtained, as shown in Fig. 6 (c). Indeed, the CFD results and experiments (Brandt & Selig, 2011) exhibited the same behavior: the efficiency increased with the advance ratio, reached a maximum, and then decreased. However, the values obtained through CFD were consistently inferior to the experimental values, and the efficiency of

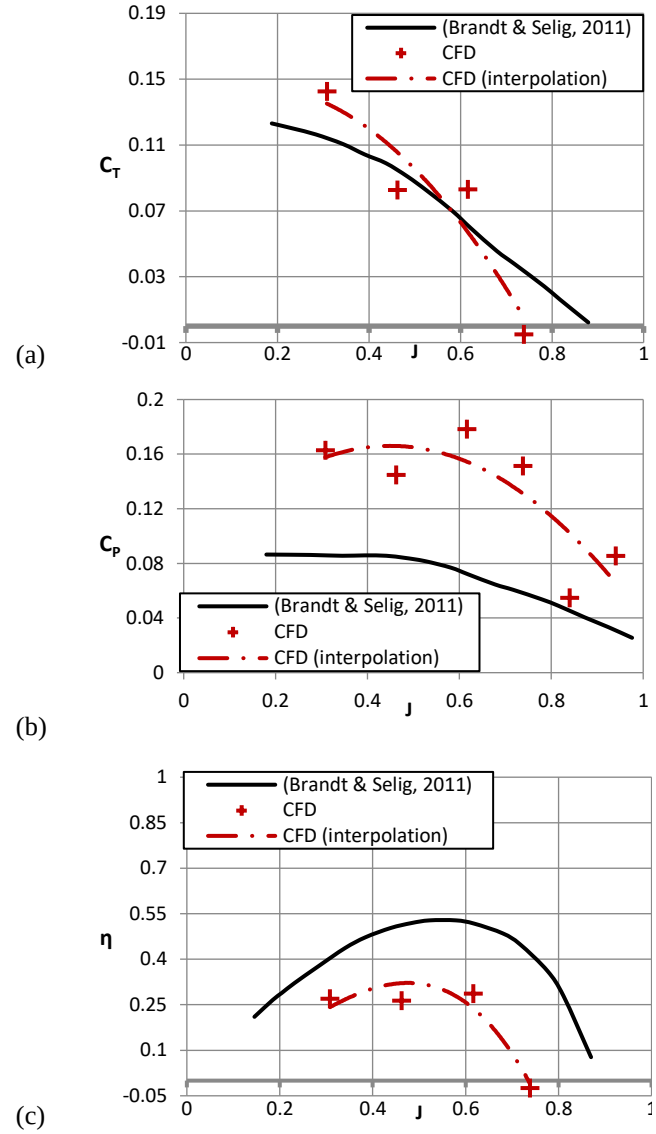

Fig. 6 Thrust (a) and power (b) Coefficients, and efficiency (c) variation with respect to the advance ratio for the isolated propeller

CFD is known (Rhee & Joshi, 2005; Su et al., 2019). Although the overall efficiency was underpredicted, the advance ratio corresponding to the maximum efficiency was close to that obtained experimentally.

Hence, although the CFD approach used cannot be validated quantitatively, it provides a good qualitative description of the efficiency behavior with a good prediction of the position of its maximum value, which corresponds to an advance ratio of approximately J=0.48 from the tendency curve, and approximately J=0.62 if the computed results are considered. Both values are close to the experimental data by approximately 13% (approximately J=0.55 from Brandt and Selig (2011)).

The considerable difference between the results obtained through the CFD simulations and experiments was mainly due to the central recirculation zone, which in turn was a consequence of hub removal. The contours of pressure and velocity allowed the identification of the zone that caused disagreement with the experiments.

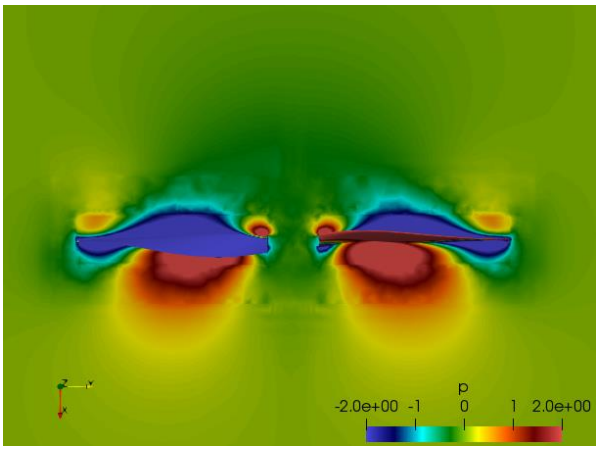

Fig. 7 Relative pressure field (in Pa) near the isolated propeller

However, as the objective of the study was only to compare the effect of spacing in the CRP configurations, the behavioral description was deemed sufficient, and the results were then only compared and interpreted in relation to each other.

Figures 7 and 8 show the pressure and velocity fields near the propeller, respectively. The bounds of the color scale were reduced to better visualize the flow structure (with the other cases having similar behaviors of the considered parameters, except for J=0.738, which is not within the scope of this study as it does not produce thrust).

The pressure field (in Pa) near the propeller is illustrated in Fig. 7. The visualized pressure is the relative pressure, with the reference being atmospheric pressure (hence, negative values indicate a decrease in pressure with respect to the reference pressure).

A lobe of underpressure was observed on the suction side of each blade, and a lobe of overpressure was observed on the pressure side of each blade. Near the root and tips, the over- and underpressure lobes were inverted, indicating the presence of vortices on both the roots and tips of the blades.

Fig. 8 (a) shows the axial velocity field (m/s) in the proximity of the propeller, with the positive direction being the free-stream direction. The air was being pushed streamwise by the propeller, as indicated by the high-velocity lobes on the pressure side of the propeller.

On the suction side of the propeller, a band of high axial velocity was observed, which was due to the airfoil characteristic of accelerating the flow on its suction side combined with the angle of attack. Regions of lower axial velocity were observed near the tips and roots of the blades, further pointing toward the existence of tip vortices.

In addition to the pressure and axial velocity fields indicating the presence of tip vortices, the change in velocity from centrifugal to centripetal is best illustrated in Fig. 8 (b), which represents the radial velocity (in m/s) field in the middle plane.

(a)

(b)

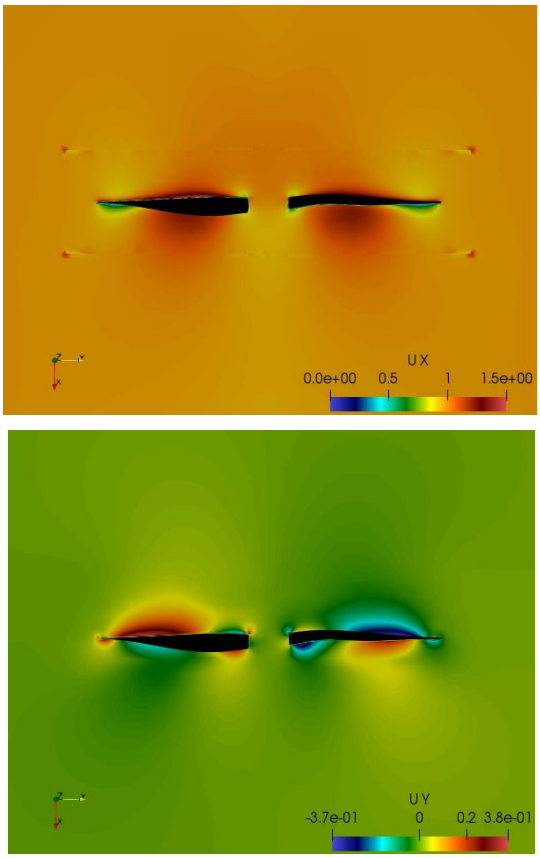

Fig. 8 Axial (a) and radial (b) velocity fields (in m/s) near the isolated propeller

An antisymmetrical field was observed between the suction and pressure sides, with air from the pressure side moving toward the tips and air from the suction side moving toward the tips. Near the roots and at the tips, the opposite behavior was observed. Note that the change in the radial velocity near the roots was more pronounced than that near the tips.

As evident from the pressure and velocity contours, the CFD simulations captured all the important phenomena associated with the propellers, except in the center, where the hub was supposed to be present. Figures. 7 and 8 show that the main reason for the considerable difference between the CFD simulations and the experimental results is the presence of a relatively large recirculation zone at the location where the hub should have been present. Thus, the removal of the hub is the main reason for the observed lack in performance and the amplification of the already known consequences of using the k–ε model.

To visualize the wake development, the contours of vorticity ω (in 1/s) are shown for different planes normal to the stream direction at the distances of 0D, 0.1D, 0.25D, and 0.5D in Fig. 9; the same scale from -1 to 1 s^{-1} was used to assess the change in intensity in addition to structures.

The vorticity shown throughout this paper is the vorticity component in the direction of the propeller's rotation (which corresponds to the "x" direction), which

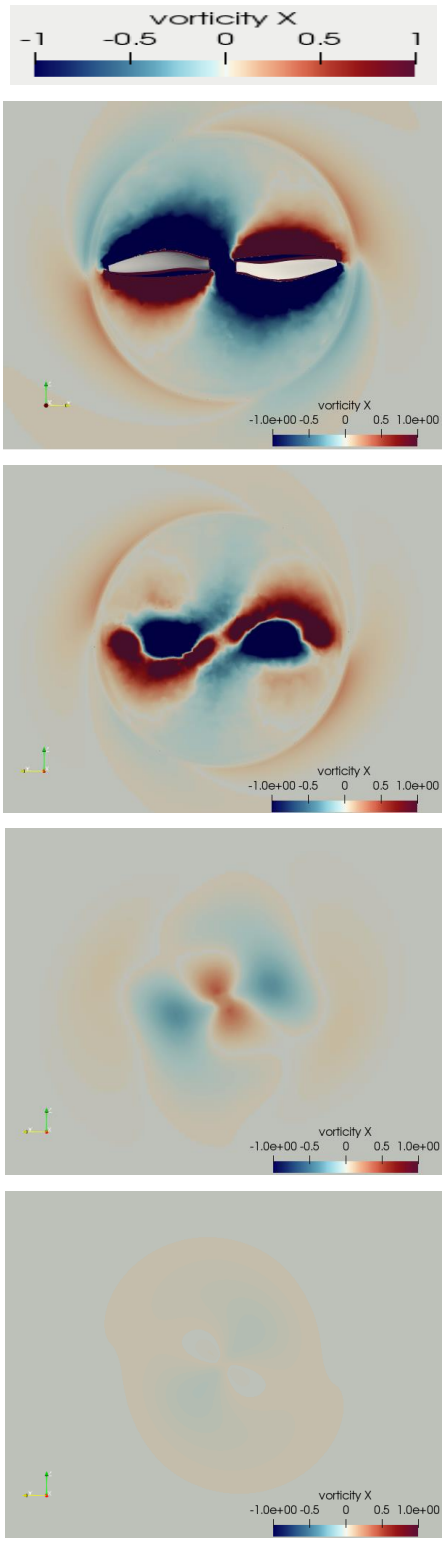

Fig. 9 Vorticity distributions (in 1/s) at different slices in the wake of an isolated propeller

facilitates the interpretation of the swirling structures induced by the propeller. Vorticity is defined as the curl of the velocity field, as shown in Equation (16) in vector notation:

$$\vec{\omega} = \vec{\nabla} \times \vec{u} \tag{16}$$

The first observation is that the vorticity field (which indicates the generated turbulence) tends toward a uniform zero state at a short distance from the propeller; indeed, at a distance of 0.5D, the field is barely perceptible.

In addition, structures indicating the presence of vortices could be observed, with the removal of the hub having a significant effect. At the proximity of the propeller (positions 0D and 0.1D), the structures followed the shape of the blades: a lobe having an "s" shape and two opposite lobes enveloped by the previous one. However, at the distances of 0.25D and 0.5D, the "s"-shaped structure separated into two distinct lobes normal to the opposite ones, making a clover-shaped pattern whose intensity decreased with distance. In the considered CRP cases, the aft propeller was placed at a distance where the clover pattern was observed.

To conclude regarding the isolated propeller case, CFD simulations using the k–ε model yielded good qualitative results with a phenomenological description of the pressure, vorticity, and velocity fields aside from abnormalities, which were purely due to the removal of the hub. Although the deviation from the experimental data was not negligible (as expected), the simulations predicted the main flow structures and physical phenomena; hence, this framework is suitable for estimating the general behavior of propellers at a lower computational cost than more intrinsically accurate models, which justifies its use in CRP cases.

4.2. Contra-Rotating Propellers

Simulations were performed for three CRP cases characterized by their interpropeller distance d. Three interpropeller distances (d) were chosen: d=0.3D, d=0.5D, and d=1.0D. The same geometry and rpm were used for both propellers. Only the flight conditions that yielded the maximum efficiency in the isolated propeller case were considered (J=0.616 with a free-stream velocity of 1 m/s).

The sustained regime was considered to have been achieved at the fifth revolution (approximately 0.95 s) because of the slow convergence toward this sustained regime. Figure 10 shows only the variation in the thrust coefficient; however, the power coefficient and efficiency exhibited the same behavior.

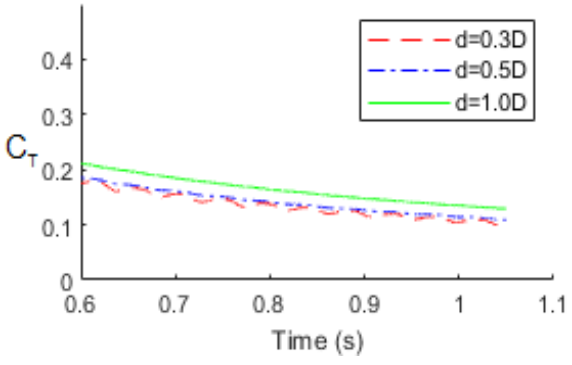

Fig. 10 Convergence curves of the thrust coefficient for different CRP configurations

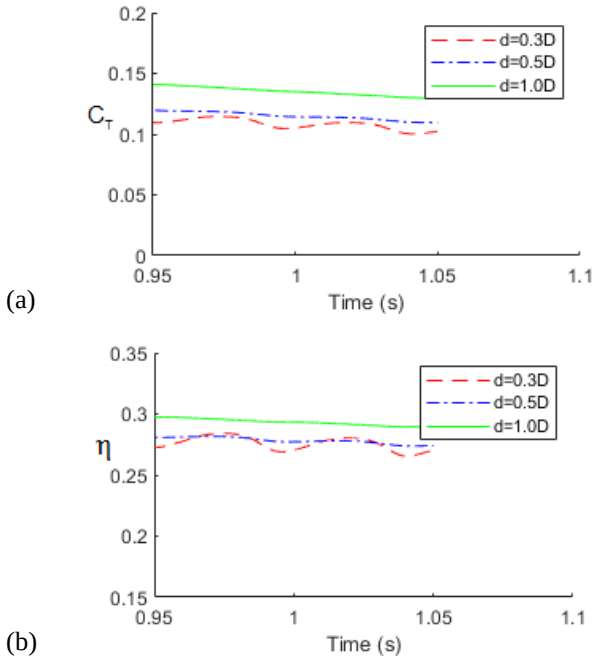

Fig. 11 Variation of the thrust coefficient (a) and efficiency (b) with respect to time in the sustained regime

Figure 11 shows the variations in the thrust coefficient and efficiency with respect to time. Oscillations were observed, with the amplitude decreasing substantially with an increase in the interpropeller distance.

Notably, the frequency of the oscillations φ was four times the propeller rotational frequency N ($\varphi = 4 \times N$).

Note also that the oscillations are a consequence of the time periodicity of the geometry found in turbomachinery (and not flow turbulence), which, in the studied case (with the same diameter, number of blades, and rpm for the forward and aft propellers), is straightforward to predict.

Although the oscillations were not turbulence induced, the Strouhal number St for the studied configurations could be defined as follows:

$$St = \frac{\varphi c_{ref}}{U_b} = \frac{4Nc_{ref}}{\frac{3}{4}\frac{D}{2}2\pi N} = \frac{16c_{ref}}{3\pi D} \quad (17)$$

Here, U_b is the velocity of the blade at the reference chord c_{ref}. In this study, a Strouhal number of $St \cong 0.142$ was obtained, which was observed to be independent of the propeller rpm in this specific type of CRP (same geometry and rpm), and can be considered sufficiently low to justify a performance study using the average quantities.

To assess the influence of spacing on the performance, the average parameters of the last revolution were considered, yielding the results depicted in Fig. 12. The thrust coefficient and efficiency of the aft propeller were slightly higher than those of the fwd propeller, as shown in Figs. 12 (a) and (c), which is expected because the aft propeller has an advantageous incoming swirling flow caused by the fwd propeller; however, the power coefficient was preserved.

The difference in efficiency was approximately 0.02 for the distances of d=0.3D and d=0.5D; however, it was negligible for d=1.0D, indicating that the wake of the fwd propeller has little to no effect on the performances of the aft propeller.

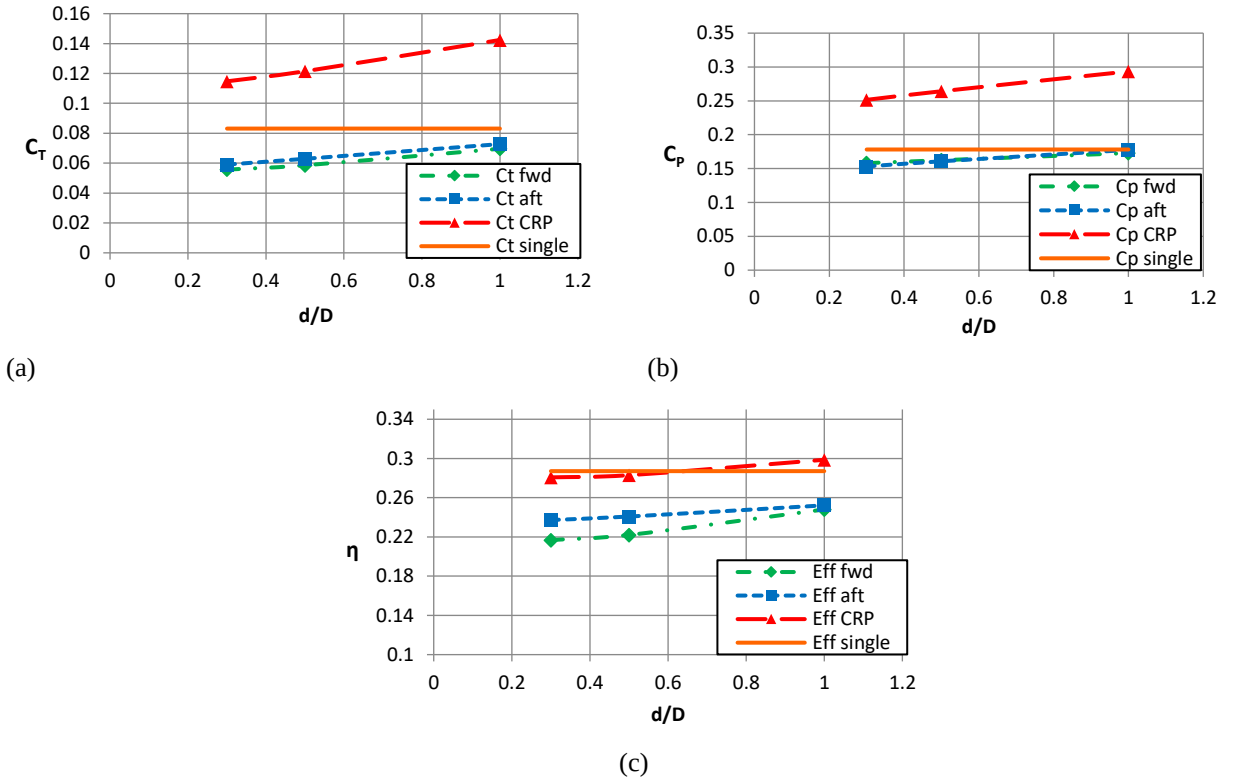

Fig. 12 Effect of the inter-propeller distance on the thrust (a) and power (b) coefficients and efficiency (c)

Other observations were related to the C_T of the fwd and aft propellers. If considered individually, they were inferior to the C_T of the isolated propeller case. However, when combined, they provided a much higher value, as shown in Fig. 12 (a). Another observation concerns the C_P of the fwd and aft propellers; if considered individually, they were inferior to the C_P of the isolated propeller for small spacing and converged toward the latter as the spacing increased. When combined, the resulting C_P was higher than that in the single-propeller case (Fig. 12 (b)).

These results are expected and can be attributed, on the one hand, to the fact that the torque of each propeller is countered by the torque of the other, thus reducing the required power to rotate each propeller, with the effect being more pronounced for shorter interpropeller distances; on the other hand, the decrease in the thrust coefficient can be attributed to the fact that the flow in the vicinity of the propeller is more turbulent with decreasing spacing.

The interaction between the two propellers (which is more prevalent for reduced interpropeller distances) reduces performance (the C_T and C_P of CRPs are not equal to twice those of a single propeller). This observed loss in performance is consistent with Xu et al. (2024).

Although the individual efficiencies of the fwd and aft propellers were lower than the efficiency of an isolated propeller, the efficiency of the entire CRP system was almost identical, as shown in Fig. 12 (c), with the efficiency being slightly inferior for the spacings of 0.3D and 0.5D, and slightly superior for the spacing of 1.0D. However, the efficiency of the CRP system is predicted to increase with an increase in the interpropeller distance. From a spacing of d=0.3D to d=1.0D, the C_T increased by 24%, the C_P by 14%, and the efficiency by 6.3%.

For the qualitative description of the physical phenomena present in CRP systems, only the case where the propeller blades were not aligned was considered. This was because, when the propellers are perfectly aligned, the pressure, velocity, and vorticity fields are nearly identical to those expected from two isolated propellers, and the interaction between the two propellers is not observed clearly.

Figure 13 shows the pressure field near each of the fwd and aft propellers for all the studied CRP configurations. The slices were taken in the fwd and aft propeller planes (the scale was set from -1 to 1 Pa for visualization purposes). The pressure fields near the propellers were almost identical in all the cases; however, differences were observed in the interpropeller region.

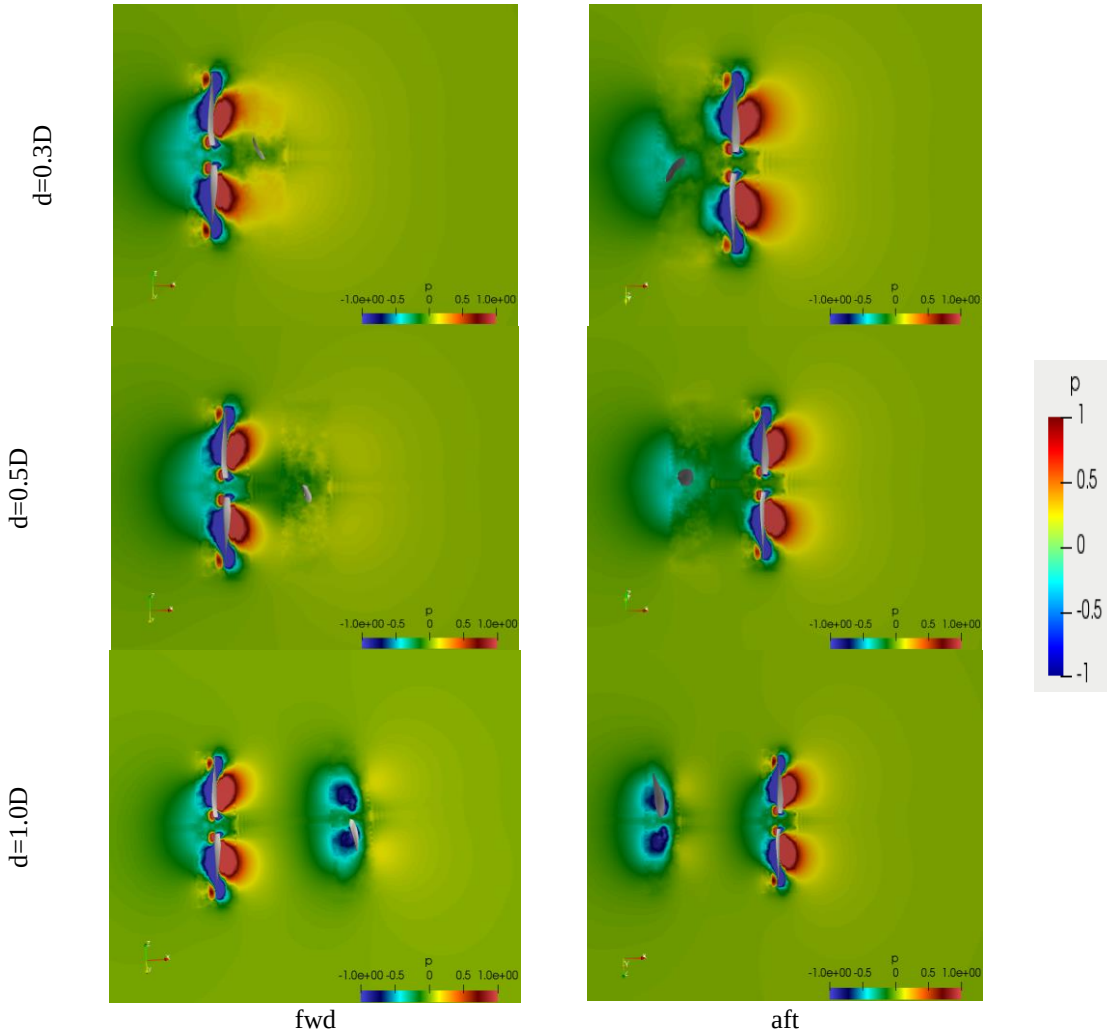

Fig. 13 Relative pressure (in Pa) distributions near the fwd and aft propellers for different CRP configurations

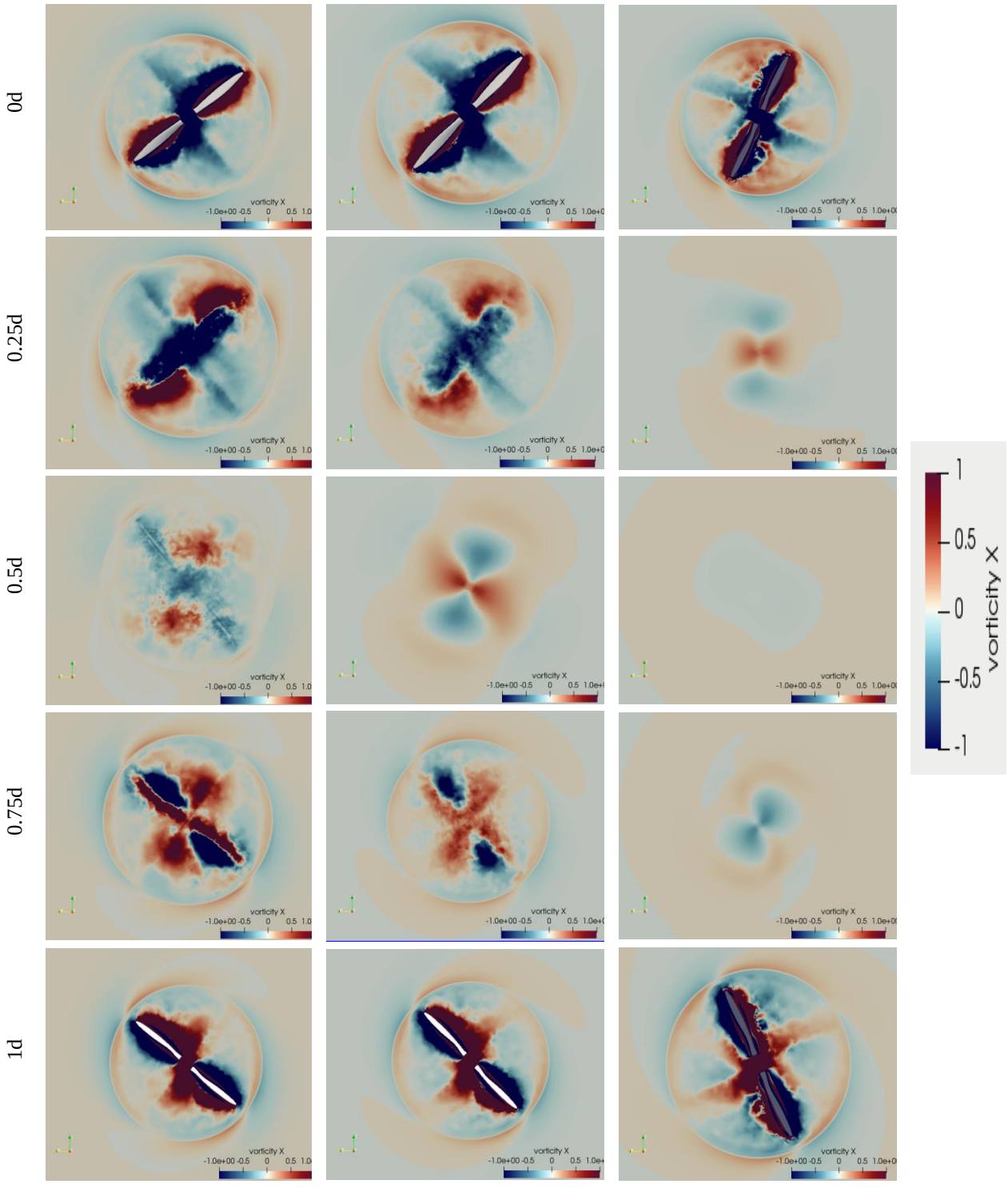

Fig. 14 Vorticity field (in 1/s) at slices in the inter-propeller region

For a spacing of d=0.3D, the overpressure lobes on the pressure side of the fwd propeller extended further downstream and were slightly directed toward the rotation axis. They created an overpressure region to which the aft propeller was subjected, and hence, the aft propeller outperformed the fwd propeller in terms of efficiency. The underpressure region induced by the aft propeller was smaller than that of the fwd propeller, and hence, even if the aft propeller demonstrated higher efficiency than the fwd propeller, the performances of the individual propellers in the CRP system were inferior to those of the isolated propeller.

For a spacing of d=0.5D, the overpressure lobes did not extend to the aft propeller; however, the underpressure region induced by the aft propeller did. However, the underpressure intensity was still lower than that of the fwd propeller. The larger underpressure region combined with the absence of the influence of the overpressure lobes caused by the forward propeller can explain why the aft propeller performed better than the forward propeller.

For a spacing of d=1.0D, no visible interaction between the propellers was observed in the pressure fields.

Figure 14 depicts the vorticity distribution in the direction of propeller rotation, where slices were taken at different positions (x) in the interpropeller region (hence, the absolute distance from the forward propeller was not the same for the compared configurations): x= 0d, 0.25d, 0.5d, 0.75d, and 1d. The same scale of vorticity was maintained to compare vortical structures and their intensity; all the slices were oriented to have a front view (x-axis pointing inward), indicating that positive values were in the direction of the forward propeller rotation (clockwise).

For the slice located at the fwd propeller, for the interpropeller distances of 0.3D and 0.5D, the vorticity distribution was similar to that of the isolated propeller; however for a spacing of 1.0D, the distribution was perturbed, and structures were thinner, although the main features were conserved (an "s"-shaped zone enveloping two inverted vorticity lobes).

At 25% of the interpropeller distance, the spacings of d=0.3D and d=0.5D exhibited the same structures, but the ones corresponding to a larger spacing had an inferior intensity. This is solely because of the increase in spacing. However, in the case having a spacing of d=1.0D, different structures were predicted; indeed, the predicted structures were similar to those predicted for the wake of the isolated propeller at the same distance (namely 0.25D). The influence of both propellers on the vorticity field was best observed at 75% of the interpropeller distance; for the configurations of d=0.3D and d=0.5D, the vortical structures could be described as a superposition of the fwd-propeller-induced structures and the aft-propeller-induced structures; indeed, the clover pattern was superimposed to the "s" pattern in those cases.

For the d=1.0D case, there was no superposition, which is characteristic of the aft propeller only; however, the slightly positive vorticity in most fields near the propeller indicates that swirl owing to the fwd propeller was still present.

Although qualitative, the results predicted an increase in efficiency with an increase in spacing. The reason for this, as expressed by the slices of the vorticity field, is the dissipation of turbulence in the wake of the fwd propeller, whereas the flow swirl induced by it was preserved.

The interaction mechanisms were studied only for three spacings, with the smaller spacing being d=0.3D Smaller spacings would have different interaction mechanisms (particularly in the pressure field), which could have a significant effect on the efficiency. Note that individual propellers perform worse than isolated propellers, but when combined, they have a similar efficiency. Therefore, more thrust can be produced while preserving the propulsive efficiency, making the CRP configuration advantageous in applications where the advance ratio is sufficiently high and weight is a major concern (as single-engine CRPs weigh less than two isolated propellers).

5. CONCLUSION

A qualitative assessment of an isolated propeller and three CRP configurations with different interpropeller distances was conducted.

The obtained results were consistent with the experimental data. We considered hub removal to be the primary factor contributing to the performance gap. Nevertheless, the performance curves demonstrated trends similar to those of the experimental findings.

Regarding the effects of the CRP interpropeller distance configurations, the performance difference between the configurations was significant, with an increased spacing leading to an improved performance.

In fact, the C_T increased by 24%, the C_P by 14%, and the efficiency by 6.3%. This improvement was best explained through vorticity analysis within the interpropeller region. The simulations predicted that the performance improvement was due to the induced swirl conservation over a longer distance compared with the turbulent structures, which dissipated close to the propeller that generated them.

ACKNOWLEDGEMENTS

The authors would like to thank the Wind Energy Aerodynamics division from the Renewable Energy Development Centre, as well as the Laboratory of Aeronautical Sciences at the University of Blida 1, for the computational resources used throughout this project.

CONFLICT OF INTEREST

The authors have no conflicts of interest to disclose.

AUTHORS CONTRIBUTION

Hocine Bentrad: Writing – review & editing, Investigation, Methodology, Resources, Visualization, Conceptualization, Supervision, Project administration; **Hamza Moulai:** Writing – original draft, Investigation, Visualization, Methodology, Formal analysis, Data curation, Software, Conceptualization; **Ahmed Bekhti:** Writing – review & editing, Methodology, Investigation, Software, Visualization, Resources, Supervision; **Sbâa Laâzab:** Writing – review & editing, Methodology, Investigation, Visualization, Software, Resources, Supervision.

REFERENCES

Azizan, N. N., & Sapit, A. (2022). Airflow characteristic of UAV Quadcopter propeller blade using computational fluid dynamics (CFD). *Progress in Aerospace and Aviation Technology, 2*(2) , 8-16. http://dx.doi.org/10.30880/paat.2022.02.02.002

Brandt, J. B., & Selig, M. S. (2011). *Propeller Performance Data at Low Reynolds Numbers* [Conference session]. 49th AIAA Aerospace

Sciences Meeting, Orlando, FLA, United States. http://dx.doi.org/10.2514/6.2011-1255

Colley, E. & Gourlay, T. (2012). Analysis of Flow around a Ship Propeller using OpenFOAM. Technical report, Curtin University Perth, Western Australia. https://cmst.curtin.edu.au/wp-content/uploads/sites/4/2016/05/colley_eamonn_2012_analysis_of_flow.pdf

Feng, F., Geng, C., Guo, T., Huang, Q. Y., & Hu, J. (2017). *Numerical Simulation of Contra Rotating Propellers* [Conference session]. International Conference on Manufacturing Engineering and Intelligent Materials (ICMEIM 2017), Guangzhou, China. https://doi.org/10.2991/icmeim-17.2017.92

Grassi, D., Brizzolara, S., Viviani, M., Savio, L., & Caviglia, S. (2010). Design and analysis of counter-rotating propellers-comparison of numerical and experimental results. *Journal of Hydrodynamics*, *22*(Suppl 1), 553-559. https://doi.org/10.1016/S1001-6058(09)60254-7

Greenshields, C. J. (2015). OpenFOAM, The Open Source CFD Toolbox, Programmer's Guide. Version 3.0.1. OpenFOAM Foundation Ltd.

Launder, B. E., & Spalding, D. P. (1974). The Numerical Computation of Turbulent Flows. *Computer Methods in Applied Mechanics and Engineering*, *3*(2), 269-289. http://dx.doi.org/10.1016/0045-7825(74)90029-2

Liu, S., Arabnejad, M., & Nilsson, H. (2017). *Implementation of a complete wall function for the standard k− ϵ turbulence model in OpenFOAM 4.0*. Technical report, University of Stavanger. https://www.tfd.chalmers.se/~hani/kurser/OS_CFD_2016/ShengnanLiu/FinalReport-Shengnan.pdf

Lopez, J., & Juando, A. (2023). *Development of standardized series of counter-rotating propellers with special interest in hydrofoil navigation* [Conference session]. 25th Numerical Towing Tank Symposium (NuTTS), Ericeira, Portugal. https://blueoasis.pt/wp-content/uploads/2023/10/Nutts2023_proceedings_v4.pdf

Pérez, G., A. M., Villegas, S., J. S., López, O. D., Suárez, C., L., & Escobar, J. A. (2019). Numerical and experimental estimation of the efficiency of a quadcopter rotor operating at hover. *Energies*, *12*(2). http://dx.doi.org/10.3390/en12020261

Rhee, S. H., & Joshi, S. (2005). Computational validation for flow around a marine propeller using unstructured mesh based navier-stokes solver. *JSME International Journal Series B, 48* (3), 562-570. https://doi.org/10.1299/jsmeb.48.562

Russo, N., Marano, A. D., Gagliardi, G. M., Guida, M., Pollito, T., & Marulo, F. (2023). Thrust and noise experimental assessment on counter-rotating coaxial rotors. *Aerospace, 10*(6). https://doi.org/10.3390/aerospace10060535

Satrio, D., Utama, I. K., & Mukhtasor. (2018). The influence of time step setting in on the CFD simulation result of vertical axis tidal current turbine. *Journal of Mechanical Engineering and Sciences*, *12*(1), 3399-3409. https://doi.org/10.15282/jmes.12.1.2018.9.0303

Silvestre, M., Morgado, J., Alves, P., Santos, P., Gamboa, P., & Páscoa, J. C. (2015). Propeller Performance measurements at low reynolds numbers. *International Journal of Mechanics, 9*(9), 154-166. https://www.naun.org/main/NAUN/mechanics/2015/a372003-136.pdf

Stajuda, M., Karczewski, M., Obidowski, D., & Jozvik, K. (2016). Development of a CFD model for propeller simulation. *Mechanics and Mechanical Engineering*, *20* (4), 579-593. https://kdm.p.lodz.pl/sites/k13/files/manual/articles/2016/4/20_4_15.pdf

Stokkermans, T. C., van Arnhem, N., Sinnige, T., & Veldhuis, L. L. (2018). Validation and comparison of RANS propeller modeling methods for tip-mounted applications. *AIAA Journal 57*(3), 1-15. http://dx.doi.org/10.2514/1.J057398

Su, S., Wang, S., Cao, J., & Feng, D. (2019). *Prediction of hydrodynamic characteristics of combined propellers based on CFD method* [Conference session]. 3rd International Conference on Fluid Mechanics and Industrial Applications. Taiyun, China. *Journal of Physics: Conf. Series 1300 012016. 29–30 June 2019, Taiyun, China.* https://doi.org/10.1088/1742-6596/1300/1/012016

Thiele, M., Obster, M., & Hornung, M. (2019). *Aerodynamic Modeling of Coaxial Counter-Rotating UAV Propellers* [Conference session]. 8th Biennial Autonomous VTOL Technical Meeting. Mesa, Arizona, United States. https://mediatum.ub.tum.de/doc/1473749/document.pdf

Triet, P. M., Thien, P. Q., & Hieu, N. K. (2018). CFD simulation for the Wageningen B-Series propeller characteristics in open-water condition using k-epsilon turbulence model. *Science and Technology Development Journal, 1* (1), 35-42. https://doi.org/10.15419/stdjet.v1i1.526

Wenhui, Y., & Kun, Z. (2023). *Effects of Stage Spacing on Contra-Rotating Propeller Aerodynamic Interactions* [Conference session]. 2022 International Conference on Defence Technology (2022 ICDT). Changsha, China. *Journal of Physics Conference Series 2478(12):122013,* https://doi.org/10.1088/1742-6596/2478/12/122013

Xu, J., Yu, J., Lu, X., Long, Z., Xu, Y., & Sun, H. (2024). Aerodynamic performance and numerical analysis of the coaxial contra-rotating propeller lift system in eVTOL vehicles. *Mathematics, 12*(7). http://dx.doi.org/10.3390/math12071056